DIRBE Comet Trails

Richard G. Arendt

CREST/UMBC, Code 665, NASA/GSFC, Greenbelt, MD 20771;
Richard.G.Arendt@nasa.gov

ABSTRACT

Re-examination of the *COBE* DIRBE data reveals the thermal emission of several comet dust trails. The dust trails of 1P/Halley, 169P/NEAT, and 3200 Phaethon have not been previously reported. The known trails of 2P/Encke, and 73P/Schwassmann-Wachmann 3 are also seen. The dust trails have 12 and 25 μm surface brightnesses of < 0.1 and < 0.15 MJy sr^{-1}, respectively, which is $< 1\%$ of the zodiacal light intensity. The trails are very difficult to see in any single daily image of the sky, but are evident as rapidly moving linear features in movies of the DIRBE data. Some trails are clearest when crossing through the orbital plane of the parent comet, but others are best seen at high ecliptic latitudes as the Earth passes over or under the dust trail. All these comets have known associations with meteor showers. This re-examination also reveals one additional comet and 13 additional asteroids that had not previously been recognized in the DIRBE data.

Subject headings: comets: individual (1P/Halley, 2P/Encke, 73P/Schwassmann-Wachmann 3, 169P/NEAT) — meteorites, meteors, meteoroids — minor planets, asteroids: individual (3200 Phaethon) — zodiacal dust

1. Introduction

The first associations between annual meteor showers and periodic comets were made in the 1860s by Schiaparelli (1867) and others. Accounts of the history of these early developments are presented by Kirkwood (1873), Littmann (1998) and Jenniskens (2006). This led to the recognition that the meteors observed in annual showers are the debris shed as comets break up and disintegrate over time with repeated passages near the sun. Over the next century, the number of associations between meteor showers and comets grew with accumulation of additional data on both comets and meteors, and with advances in the computational capabilities in determining the perturbations and evolution of orbits of short period comets and associated meteoroid streams (Jenniskens 2006, and references therein).

A fundamentally new phase of this research began in 1983 with the launch of the *Infrared Astronomical Satellite* (*IRAS*, Neugebauer et al. 1984). *IRAS* performed the first full-sky survey at mid-IR wavelengths of 12, 25, 60, and 100 μm. At these wavelengths, particularly 12 and 25 μm, the observations are very often dominated by the thermal emission of interplanetary dust, or zodiacal light. The orbits of interplanetary dust grains are not stable, with the grains slowly spiraling inward under the influence of Poynting-Robertson and solar wind drag, and radiation pressure (Burns et al. 1979; Ipatov et al. 2008). Therefore it had been recognized that the interplanetary dust needs to be continually replenished from new sources of dust. *IRAS* provided clear evidence for replenishment by main belt asteroids with the discovery of "bands" at low ecliptic latitudes (Low et al. 1984; Sykes 1988; Nesvorný et al. 2006). *IRAS* also provided evidence of replenishment by comets with "the discovery of dust trails in the orbits of periodic comets" (Sykes et al. 1986). With *IRAS* it became possible to *see* the dust trails of debris that is shed from comets. These trails provide a means of detecting and quantifying (nascent) meteoroid streams even in cases where the streams do not intersect or approach Earth's orbit (Sykes & Walker 1992). Later space-based IR observatories, *ISO* and *Spitzer*, have discovered additional dust trails and have provided observations with greatly improved spectral and spatial resolution. Recently, dust trails have also been detected at optical wavelengths with ground-based instruments (Ishiguro et al. 2009).Earth These studies provide detailed characterization of dust grain size and composition, and on the total masses of the trails (e.g. Sykes et al. 1990; Reach et al. 2007, 2009; Vaubaillon & Reach 2010).

In 1989-90 the Diffuse Infrared Background Experiment (DIRBE) on the *Cosmic Background Explorer (COBE)* satellite, like *IRAS*, also performed a full-sky survey at mid-IR wavelengths (Hauser et al. 1998). DIRBE was designed for measurement of the cosmic IR background, and to provide complementary observations to the microwave background experiments on *COBE*. Therefore it was designed with the capability of making absolutely calibrated brightness measurements over a wide range of solar elongations, but with low angular resolution. Several of the brightest comets in the inner solar system were detected by DIRBE, but no dust trails of these or other comets were identified (Lisse et al. 1998).

Despite this negative result, the recent dusty demise of comet ISON (Knight & Battams 2014) has inspired a reinvestigation of the DIRBE data to see if there might be a detectable dust trails associated with other sun-grazing comets. In particular, the Kreutz family sun-grazers (Marsden 1989, 2005) seemed like a likely candidate for having an old dust trail formed from multiple past break ups, as well as a new dust trail forming from the disintegration of the hundreds of small comets witnessed by the *Solar & Heliospheric Observatory (SOHO)* and other solar coronagraphic satellites over the past decades (Knight et al. 2010).

The results of an initial reinvestigation of the DIRBE data are reported here. Section 2 of this paper provides a brief overview of the DIRBE data, and describes the specific data reduction steps that were taken that greatly enhance the detection of faint moving objects and structures in the solar system. Section 3 summarizes asteroids and comets that are newly revealed in the DIRBE data. Section 4 provides a guide to the comet dust trails that are now evident in the DIRBE data. A key aspect of recognizing the dust trails is the inspection of animations of daily images of the IR sky brightness after removal of bright large-scale zodiacal light. The discussion in Section 5 includes the basic characterization of the width and brightness of the dust trails, and limitations on DIRBE's ability to detect trails. It also describes associations between the trails and meteor showers, and discusses possibilities for further improvements in reducing the DIRBE data for the purpose of detecting dust trails. The paper is summarized in Section 6.

2. DIRBE Data

The DIRBE instrument was built to measure the absolute brightness of the entire sky at $\sim 0.7°$ resolution in 10 broad bands at $\lambda = 1.25$, 2.2, 3.5, 4.9, 12, 25, 60, 100, 140, and 240 μm. The DIRBE beam was set at a 30° angle from the spacecraft spin axis, and thus traced a 60° diameter circle on the sky with each 0.8 rpm rotation of the spacecraft. The *COBE* spin axis was kept pointing near the local zenith (at a solar elongation of $\sim 94°$) as the spacecraft orbited in a polar orbit with a period of 103 min. In a single orbit the DIRBE beam would therefore trace a cycloidal path over a viewing swath covering solar elongations $64° \lesssim \epsilon \lesssim 124°$. The coverage of this swath is sparse for a single orbit, but is fairly complete after a full day (though still shallow). Averaging data on a weekly timescale produces high quality images of the viewing swath, but can hide details of the changing zodiacal light and moving solar system objects. The accumulation of sky coverage by DIRBE is nicely illustrated by Figure 1 of Kelsall et al. (1998). Nominal cryogenic operations of all the DIRBE bands lasted for 285 days ($\sim 3/4$ yr), which was sufficient to obtain complete coverage of the full sky, but not with the uniformity that a full year of operation would have provided. Details of the DIRBE instrument can be found in Silverberg et al. (1993), Hauser et al. (1998), and the DIRBE Explanatory Supplement[1]. Information on the *COBE* spacecraft and mission is presented by Boggess et al. (1992).

The reprocessing of the DIRBE data for the present analysis began with the Calibrated Individual Observations. For the appropriate time and location of each observation, the

---

[1]http://lambda.gsfc.nasa.gov/product/cobe/dirbe_exsup.cfm

Kelsall et al. (1998) model of the zodiacal light was calculated for all DIRBE bands. The observations of each day were averaged into separate sky maps with and without subtraction of the zodiacal light. Observations within 10° of the moon were excluded from the averages. These zodiacal light subtracted images are not well suited for detection of faint structure and moving objects because they still contain the Galactic background and residuals of the zodiacal light subtraction. At $\lambda \geq 12$ μm the Galactic background is dominated by thermal emission of dust in the ISM, while at $\lambda \leq 4.9$ μm stellar sources dominate. Most of the residual zodiacal light emission retains a relatively fixed pattern with respect to elongation and ecliptic latitude, modulated by a slower evolution of this pattern during the mission.

To mitigate these variations, the time series of observations were filtered to remove the lowest frequency components. The time series at each pixel was fit by:

$$I_\nu = A_0 + A_1 \cos\left(2\pi t\right) + B_1 \sin\left(2\pi t\right) + A_2 \cos\left(2\ 2\pi t\right) + B_2 \sin\left(2\ 2\pi t\right) \tag{1}$$

where time t is measured in years. The derived coefficients correspond to the real and imaginary amplitudes of the first 3 terms in the Fourier decomposition of the variation at each pixel. Tests were done subtracting additional higher frequency components, or separately fitting observations in the leading or trailing halves of the orbit, or with different functional (e.g. polynomial) forms. However, these more complex versions were not used because further improvements were small, additional artifacts were introduced, and/or the additional degrees of freedom in the fit began to remove real features of interest. Another alternate test of this technique was to apply the fit to the data without prior subtraction of the zodiacal light model. This works fairly well as an ad hoc zodiacal light subtraction at high latitudes, but still leaves substantial residuals at low latitudes where the zodiacal light is brighter and more structured. Figures 1 and 2 illustrate the effectiveness of the removal of the temporal variations at 12 and 25 μm for representative pixels at various ecliptic latitudes. The original variations are shown along with the different versions of zodiacal light and fit subtracted results.

Subtraction of the zodiacal light and the fit from each pixel makes significant improvement in flatness of the residual images. The constant term in the fit is very effective at removing the diffuse Galactic emission. However, bright point sources still leave residuals because the square shape and sharp edges of the DIRBE beam, combined with the variable scan direction when crossing a given source, induce an irregular high-frequency variability in pixels at the edges of the sources. This is the biggest limiting factor in the short wavelength images, $\lambda \leq 4.9$ μm, which will not be discussed in further detail here. At wavelengths $\lambda \geq 60$ μm residual calibration defects cause temporal drifts to map into large angular scale structure matching the scan pattern. This limits the usefulness of the these data at the present time. Thus the remaining analysis performed here utilizes the 12 and 25 μm results.

These wavelengths are where the emission of interplanetary dust is brightest and has the highest contrast with respect to the Galactic background.

At each wavelength, the sets of daily images were assembled into movies of the sky over the 285 days of the cryogenic mission. Movies in the native COBE sky cube format[2] (Greisen et al. 2006) offer the most accurate representation of the data (Figure 3a-d), and are good for examining features that are at either moderately low or moderately high latitudes ($|\beta| \lesssim 30°$ or $|\beta| \gtrsim 60°$). The initial identifications of most objects and trails were made in these movies, as described in the following sections. The still frame in Figure 3 shows the ecliptic coordinates superimposed on a single daily image in the sky cube projection.

Movies of the daily images transformed into polar projections also prove useful (Figure 4a-b). These are especially good for tracing the full extent of trails when they span a large range in latitude, thus being interrupted at the boundaries between the equatorial and polar cube faces in the sky cube projection. The weakness of the polar projected movies is that they do no clearly show features at very low ecliptic latitudes. The still frame in Figure 4 shows the ecliptic coordinates superimposed on a single daily image in the polar projection.

Each of the movies is produced in a bare version and an annotated version. The annotated versions include labels tracking the positions of asteroids and comets that can be seen at some point in the data. Labels similarly mark the locations of the bodies with associated dust trails, although these bodies are not detected except for 73P / Schwassmann-Wachmann 3. The projected orbits of the bodies with associated dust trails are marked with + symbols at 1-day increments along the orbits. The perihelions are marked with larger solid dots. Points at mean anomalies of 90°, 180° (aphelion) and 270° are marked as "1", "2", "3".

3.   Moving Objects

Close inspection of the 12 and 25 μm DIRBE movies reveals more than 20 moving solar system objects. Mars, Jupiter, and Saturn are obvious bright sources. Uranus is present in the DIRBE data, but it is not seen as a moving object in the movies. The four comets studied by Lisse et al. (1998) are easily seen, and an additional comet, C/1989 T1 (Helin-Roman-Alu), can be seen passing across the north ecliptic pole (NEP) from the start of the mission until day 90066[3]. The remaining moving objects are asteroids. Most are only visible

---

[2]http://lambda.gsfc.nasa.gov/product/cobe/skymap_info_new.cfm

[3]DIRBE day numbers are formatted as a 2-digit year + a 3-digit day of year; 90066 = the 66th day of 1990 = 1990 Mar 07

for a fraction of the time that they are within the DIRBE viewing swath.

These solar system objects are listed in Table 1 and are their locations are noted in the annotated DIRBE movies. No flux densities were extracted for these objects because more accurate photometry can be obtained from older *IRAS* or newer *WISE* data, and because photometry is better done in the time domain (e.g. Lisse et al. 1998; Smith et al. 2004), than in the daily averaged images constructed here.

The orbital data for all moving objects in the study were obtained from the JPL Horizons system (Giorgini et al. 1996). Ephemerides were generated for tracking the locations of specific moving objects during the DIRBE mission, and orbital elements were used for plotting orbits projected onto DIRBE data.

4. Comet Trails

Trails were expected to be most prominent when viewed from the plane of the comet orbit (when the Earth passes the line of nodes). However, trails were also found to be visible at high latitudes as the Earth crosses above of below the comet orbit at ~ 1 au (see Fig. 5). The following text (summarized in Tables 2 and 3) describes when and where the dust trails reported here can be seen in the DIRBE data.

4.1. 1P/Halley

This dust trail is brightest, and most easily identified, in the direction of the tangent point along the orbit when passing the descending node of the orbit near day 90140. Prior to that, from as early as day 90126, the trail can be seen very faintly sweeping across the south ecliptic pole (SEP) as the Earth crosses over the trail. (See the cutout movie Figure 4c.)

The opposite node and crossing were not observed by DIRBE. At the ascending node, the Earth is inside Halley's orbit, thus the orbit is projected as a great circle and there are no tangent points. When crossing under Halley's trail, the distance is greater than when crossing over the trail. Thus the trail is not expected to appear as bright at either of these times.

4.2. 2P/Encke

The dust trail of 2P/Encke sweeping across the SEP from day 90143 to 90211 is the most obvious of the dust trails. It is also very asymmetric. It appears to be sharply bounded on the inside, at smaller heliocentric distances, but outside of the orbit it appears to fade slow into the background over a distance of $> 10°$. (See the cutout movie Figure 4d.) The crossing under 2P/Encke's orbit was not observed by DIRBE, but is likely to be similarly prominent.

When passing through the descending node of the orbit, the entire orbit lies at low elongations ($\epsilon < 64°$) and thus could not be observed by DIRBE. When passing through the ascending node near day 90240, the trail may be visible for a few days when passing through the plane, but only on the northern side of the orbit. Confusion with the Galactic plane and residual zodiacal light is lower in the north than in the south part of the orbit, but the proximity to 2P/Encke is likely to be more important in making the northern portion more visible.

4.3. 73P/Schwassmann-Wachmann 3 (SW3)

This trail is first evident following day 90084, along the orbit immediately behind 73P/SW3. It is most visible as Earth crosses under the orbit (the trail sweeps across the NEP) near day 90134. (See the cutout movie Figure 4e.) The trail fades but it remains marginally visible up until day 90152 when the Earth passes the descending node.

Passage through the ascending node was not observed by DIRBE, but would be projected as a great circle and distant, and thus would likely be faint. The Earth crosses over the orbit of 73P/SW3 at day 90212, however the trail is not visually evident at the this time. At this point the trail is ~ 3 times more distant than when the Earth crosses under the trail. The trail might be detected here by averaging along its expected location, but the significance is low.

4.4. 169P/NEAT

The trail of 169P/NEAT is evident both when Earth crosses above and below the trail. It is fainter than the trail of 2P/Encke, but it also seems to have a similar asymmetric profile. (See the cutout movies Figures 4f-g.)

The trail is not evident when projected as a great circle as Earth passes the ascending

node on day 90076. When passing the descending node at day 90262, nearly the entire orbit lies at solar elongation, $\epsilon < 64°$. One of the tangent points is barely within the viewing swath, but is too confused by residual zodiacal light artifacts to be detected.

4.5. 3200 Phaethon

The sweep of Phaethon's trail across the NEP as the Earth passes underneath is not evident, but this is probably because the apparent daily motion is so fast that the trail gets averaged away and/or smeared when constructing daily images. Shortly afterwards the trail brightens dramatically as the Earth passes through the orbital plane at the descending node on day 89351. (See the cutout movies Figures 4h.) At this time it appears that both the near and far sides of the orbit are visible, especially at 25 μm (Fig. 4b). The entire orbit lies at low elongation ($\epsilon < 64°$) when passing through the ascending node. DIRBE did not observe when the Earth crosses back under Phaethon's trail, but prior to this the trail is faintly detected sweeping northward from day 90234 until the end of the cryogenic mission on 90264. (See the cutout movies Figures 4i.)

5. Discussion

5.1. Characterization of the Dust Trails

The portions of the orbits where the dust trails appear to be visible are illustrated in Figure 6. DIRBE's elongation limit of $\epsilon > 64°$ general truncates the minimum heliocentric radius at which trails can be detected. The limits on the maximum heliocentric radius are very subjective because the trails fade smoothly with respect to time and position until they are lost in the confusion of the residual background. Additionally, at the larger radii, the proper motions of the visible trails are smaller and the viewing angles often become nearly tangent to the orbit, which means that a large range in radius is mapped into a very small location on the sky.

Quantifying the brightness and geometry of the comet trails requires averaging the emission over the length of the trail (or a fraction thereof) and as seen over several daily images. To facilitate such measurements, for each trail the daily images were reprojected into a cartesian coordinate system in which the x coordinate is angular distance from the perihelion as measured along the orbit, and the y coordinate is the angular distance perpendicular to the orbit. Mean profiles perpendicular to the trails were then generated by averaging these images over a range of angular distance and a period of time selected for good visibility of

the trails. These intervals are subsets of the full range of when and where the trails are visible. The mean profiles at 12 and 25 μm for each trail are shown in Figures 7 and 8.

The mean profiles were characterized by fitting them with a Gaussian function and a second order polynomial background

$$I_\nu(\theta) = I_0 \exp\left[-0.5(\theta - \theta_0)^2/\sigma_\theta^2\right] + C_0 + C_1\theta + C_2\theta^2. \tag{2}$$

These fits are shown in Figures 7 and 8 and the derived parameters are listed in Table 4. The table lists the dates and the length of the trail averaged to generate the profile. The approximate ranges in the line of sight angle with respect to the orbital plane (θ_{LOS}) and the mean anomaly of the trail for the length averaged are cited.[4] In detail, these ranges vary during the period integrated. The profiles for the trails of 2P/Encke and 3200 Phaethon were measured at second epochs and are tabulated, but the visibility of the trails at these times is poor. The profile of 169P/NEAT was not well fit by this parameterization because it is too broadly asymmetrical.

For all fits, control tests were performed by reflecting each orbit across the ecliptic plane, (multiplying the latitude, β, by -1) and then repeating the averaging and fitting of the data along the reflected orbit. This process samples identical dates, elongations, and latitudes (in absolute value), but at locations where no trails should be present. None of the tests exhibited any indication of a trail, i.e. a resolved gaussian profile above the background variations. This confirms that the profiles shown in Figures 7 and 8 are very unlikely to be random or the result of systematic artifacts.

The peaks of the trail profiles are offset from the orbit of the parent body by $\theta_0 < 1°$. The 1σ dimension of the profiles is typically $\sigma_\theta \sim 1.5°$, corresponding to a full width at half maximum $FWHM = 2.355\sigma_\theta \approx 5.9°$. The trails appear to be resolved, because the measured width of bright point sources is only $\sigma \approx 0.28°$ (Gaussian fit). However, some of the apparent width of the trails might be caused by the apparent motion of the trail (changing parallax) during the course of a day.

The mean color of the peak emission of the observed trails is found to be $I_\nu(25\mu\text{m})/I_\nu(12\mu\text{m}) = 1.8 \pm 0.5$. The uncertainty listed here is the dispersion between the six successful fits listed in Table 4. The estimated uncertainty in the measurement of each of the flux ratios is similar, assuming $\sim 15\%$ uncertainties on the amplitudes of the Gaussian fits. After applying the appropriate broadband color corrections, the flux ratios correspond to a blackbody dust temperature of $T = 281 \pm 34$ K, which is close to the dust temperature of 286 K at 1 au,

---

[4]Here θ_{LOS} is defined on the range of $0 - 90°$, and can be roughly estimated from $||\beta| - \theta_{LOS}| \leq |i|$ where β is the observed ecliptic latitude of a point on the orbit and i is the orbital inclination.

as in the Kelsall et al. (1998) model. This result is to be expected, given that these trails are primarily detected when closer than ~ 0.2 au (see Tables 2 and 3). The colors of the trails are therefore similar to the of emission other substructures in the zodiacal light: the Earth-resonant ring and blobs at 1 au, and the migrating asteroidal dust bands (specifically, the inwardly drifting dust when seen at high latitudes).

The peak intensity of the trails is $\lesssim 1\%$ of the intensity of the zodiacal light at high latitudes. Given the similar dust temperatures, the trails thus have column densities that are $\lesssim 1\%$ of the zodiacal dust cloud. However the observed trails are very limited in extent, and therefore constitute a far smaller fraction of the total mass of the zodiacal dust.

5.2. Trails and Meteor Showers

The 5 trails detected by DIRBE make 7 close approaches to the Earth's orbit during the period of observations. The closest approaches occur near the times the orbits cross Earth's orbit (Fig. 5) and/or when the orbits intersects the ecliptic plane. At 5 of these close approaches there are associated meteor showers that have been previously linked to the parent bodies. These showers are listed in Tables 2 and 3. The only close approach that does not have an associated meteor shower (73P/SW3 at day 90212) is relatively distant ($\Delta \gtrsim 0.17$ au) and no dust trail was visible at the time.

The DIRBE images were examined with particular attention to the parent bodies of the Quadrantid, Perseid, and Leonid meteor showers. However with the present processing no dust trails could be seen. The detection of the associated trails may be hampered by less favorable viewing geometries, and, in the case of the Leonids, a dust trail that is not fully dispersed along the entire orbit of the parent body.

No dust trail was evident along the orbit of the Kreutz family comets [e.g. C/1965 S1-A (Ikeya-Seki)] which initially motivated this study. This is likely because the orbits of these comets are highly inclined ($i = 141.8°$) to the ecliptic. Therefore any trail is nearly 1 au distant when viewed toward the SEP, and never closer than ~ 0.6 au at lower solar elongations. These minimum distances are far greater than those of any dust trails detected by DIRBE so far.

In general the trails that are detected are found at large distances (mean anomalies) from their parent bodies, and thus one might regard them as meteoroid streams rather than more traditional dust trails. An exception is the dust trail observed for 73P/SW3, which is only seen in relatively close association with (and trailing) the parent comet. It is interesting to note that these DIRBE observations show that 73P/SW3 had a prominent

dust trail prior to its breakup in 1995 at its next perihelion passage (Crovisier et al. 1996). The trail observed by Reach et al. (2009) with *Spitzer* in 2006 is ~ 6 times brighter than the DIRBE measurement at 24 μm, although this comparison may be strongly influenced by the large difference in angular resolution. *Spitzer* observations of the dust trail of 2P/Encke (Reach et al. 2007) are similarly bright compared to the DIRBE measurements reported here, though the DIRBE observation are much more distant from the comet.

The portions of the trail of asteroid 3200 Phaethon that are seen moving near the ecliptic poles are also relatively far from the parent body. However, when crossing the line of nodes near Day 89351, the trail along a distant portion of the orbit appears to be visible, especially at 25 μm. Phaethon is embedded within this segment (Fig. 6a), although too faint to detect with DIRBE. Recent reports of ongoing dust ejection from Phaethon (Li & Jewitt 2013; Jewitt et al. 2013) have noted strong activity for short intervals (a few days) immediately after perihelion. Since Phaethon is nearer aphelion during the DIRBE observations, the trail segments seen here are likely only constraints on past (though perhaps recent) dust production, rather than evidence of active ongoing dust production.

5.3. Future Prospects

This paper is only an introduction to the possibilities of using the DIRBE data for the study of comet dust trails. The techniques presented above are sufficient to find the brightest dust trails, but there are several lines of investigation that may lead to more accurate and sensitive measurement of these and other trails. For example:
(1) Ideally one would perform this analysis after subtraction of a perfect model of the emission from the main interplanetary dust cloud of cometary and asteroidal dust. Alternate models of the zodiacal light that might yield improved results have been presented by (e.g.) Wright (1998) and Rowan-Robinson & May (2013).
(2) Lacking a perfect zodiacal light model, some additional ad hoc removal of residual emission is still likely to improve the visibility of the comet trails. There are many other ways that the residual images could be filtered or processed to remove residual zodiacal light and instrumental effects. However, any such processing schemes must be careful to avoid removing the emission of the trails along with the unwanted artifacts. It may be that such processing needs to be altered on a case by case basis, optimized for each particular trail.
(3) At the shorter wavelengths (≤ 4.9 μm), residual artifacts at the edges of bright point sources are a major limitation to recognizing low surface brightness structures. This issue could be attacked with modified map-making procedures. Super-resolved images may allow more detailed and accurate mapping of each point source, though this would dilute the

effective coverage (depth) of the images. Conversely, the images could be mapped at (or convolved to) sufficiently low resolution, such that details of the beam shape are irrelevant to the reconstruction of the images.

(4) Alternately, one may forego map-making altogether and extract information on the dust trails directly from the time domain data. An advantage to this approach is that it would avoid the daily averaging of the trails, which may artificially broaden and weaken the trails, especially in cases where their proper motion is high. The disadvantage here is that in the time domain it may be difficult to find depictions of the data that clearly show the trails, or that could be used to search for additional trails.

(5) More focussed attention could be paid to non-Earth-crossing comets and trails. These trails would general appear (approximately) as great circles, with low inclinations. Throughout the year, they would always appear as bands at low to moderate ecliptic latitudes, where they could easily be confused with the brighter asteroidal dust bands.

The DIRBE results presented here suggest that dust trails may be more prevalent than previously expected. Searches for trails in archival data sets should not be limited to looking near the parent bodies, but should also focus on (a) times when the trails are especially close to the Earth's orbit, and projected at high ecliptic latitudes in the case of Earth-crossing objects, and (b) the possibility of detecting structures that may be $> 1°$ in width. In all cases, the data reduction must take care that the signal from very extended, low surface brightness, *and moving* emission is not accidentally removed.

6. Summary

The DIRBE data have been reprocessed for the purpose of looking for comet dust trails. The current procedure creates average images on a daily basis rather than a weekly basis. These images have zodiacal light subtracted according to the Kelsall et al. (1998) model, and have an additional subtraction of the slow temporal variation (12 and 6 month periods) of the residual emission and fixed background. Animations of these daily images are effective for identifying moving sources within the solar system, including faint objects (asteroids and comets) and low surface brightness structures (dust trails) that are difficult to identify in a single image. One comet and 13 asteroids were found, in addition to the 4 comets and 3 asteroids that had been previously noted. Five new and existing comet dust trails are observed by DIRBE, each associated with Earth-crossing objects, which have perihelions $q < 1$ au. The trails are most clearly seen when closest to the Earth orbit, and at moderate to high ecliptic latitude. Some of these trails can be seen far from their parent comets (or asteroid). All the trails are associated with parent bodies of established meteor showers,

although not all major meteor showers have evident IR emission. Further work on DIRBE data should be able to extend wavelength coverage, and may be able to reveal additional fainter trails.

Facility: COBE (DIRBE).

REFERENCES

Boggess, N. W., Mather, J. C., Weiss, R., et al. 1992, ApJ, 397, 420

Burns, J. A., Lamy, P. L., & Soter, S. 1979, Icarus, 40, 1

Crovisier, J., Bockelee-Morvan, D., Gerard, E., et al. 1996, A&A, 310, L17

Giorgini, J. D., Yeomans, D. K., Chamberlin, A. B., et al. 1996, in Bulletin of the American Astronomical Society, Vol. 28, AAS/Division for Planetary Sciences Meeting Abstracts #28, 1158

Greisen, E. W., Calabretta, M. R., Valdes, F. G., & Allen, S. L. 2006, A&A, 446, 747

Hauser, M. G., Arendt, R. G., Kelsall, T., et al. 1998, ApJ, 508, 25

Ipatov, S. I., Kutyrev, A. S., Madsen, G. J., et al. 2008, Icarus, 194, 769

---

[5]http://idlastro.gsfc.nasa.gov

[6]http://www.boulder.swri.edu/~buie/idl/

Ishiguro, M., Sarugaku, Y., Nishihara, S., et al. 2009, Advances in Space Research, 43, 875

Jenniskens, P. 2006, Meteor Showers and their Parent Comets (Cambridge: Cambridge Universty Press)

Jewitt, D., Li, J., & Agarwal, J. 2013, ApJ, 771, L36

Kelsall, T., Weiland, J. L., Franz, B. A., et al. 1998, ApJ, 508, 44

Kirkwood, D. 1873, Comets and Meteors: Their Phenomena in All Ages; Their Mutual Relations; and the Theory Of Their Origin (Philadelphia: J.B. Lippincott & Co.)

Knight, M. M., A'Hearn, M. F., Biesecker, D. A., et al. 2010, AJ, 139, 926

Knight, M. M., & Battams, K. 2014, ApJ, 782, L37

Li, J., & Jewitt, D. 2013, AJ, 145, 154

Lisse, C. M., A'Hearn, M. F., Hauser, M. G., et al. 1998, ApJ, 496, 971

Littmann, M. 1998, The Heavens on Fire (Cambridge: Cambridge University Press)

Low, F. J., Young, E., Beintema, D. A., et al. 1984, ApJ, 278, L19

Marsden, B. G. 1989, AJ, 98, 2306

—. 2005, ARA&A, 43, 75

Nesvorný, D., Sykes, M., Lien, D. J., et al. 2006, AJ, 132, 582

Neugebauer, G., Habing, H. J., van Duinen, R., et al. 1984, ApJ, 278, L1

Reach, W. T., Kelley, M. S., & Sykes, M. V. 2007, Icarus, 191, 298

Reach, W. T., Vaubaillon, J., Kelley, M. S., Lisse, C. M., & Sykes, M. V. 2009, Icarus, 203, 571

Rowan-Robinson, M., & May, B. 2013, MNRAS, 429, 2894

Schiaparelli, M. J. V. 1867, Astronomische Nachrichten, 68, 331

Silverberg, R. F., Hauser, M. G., Boggess, N. W., et al. 1993, in Society of Photo-Optical Instrumentation Engineers (SPIE) Conference Series, Vol. 2019, Infrared Spaceborne Remote Sensing, ed. M. S. Scholl, 180–189

Smith, B. J., Price, S. D., & Baker, R. I. 2004, ApJS, 154, 673

Sykes, M. V. 1988, ApJ, 334, L55

Sykes, M. V., Lebofsky, L. A., Hunten, D. M., & Low, F. 1986, Science, 232, 1115

Sykes, M. V., Lien, D. J., & Walker, R. G. 1990, Icarus, 86, 236

Sykes, M. V., & Walker, R. G. 1992, Icarus, 95, 180

Vaubaillon, J. J., & Reach, W. T. 2010, AJ, 139, 1491
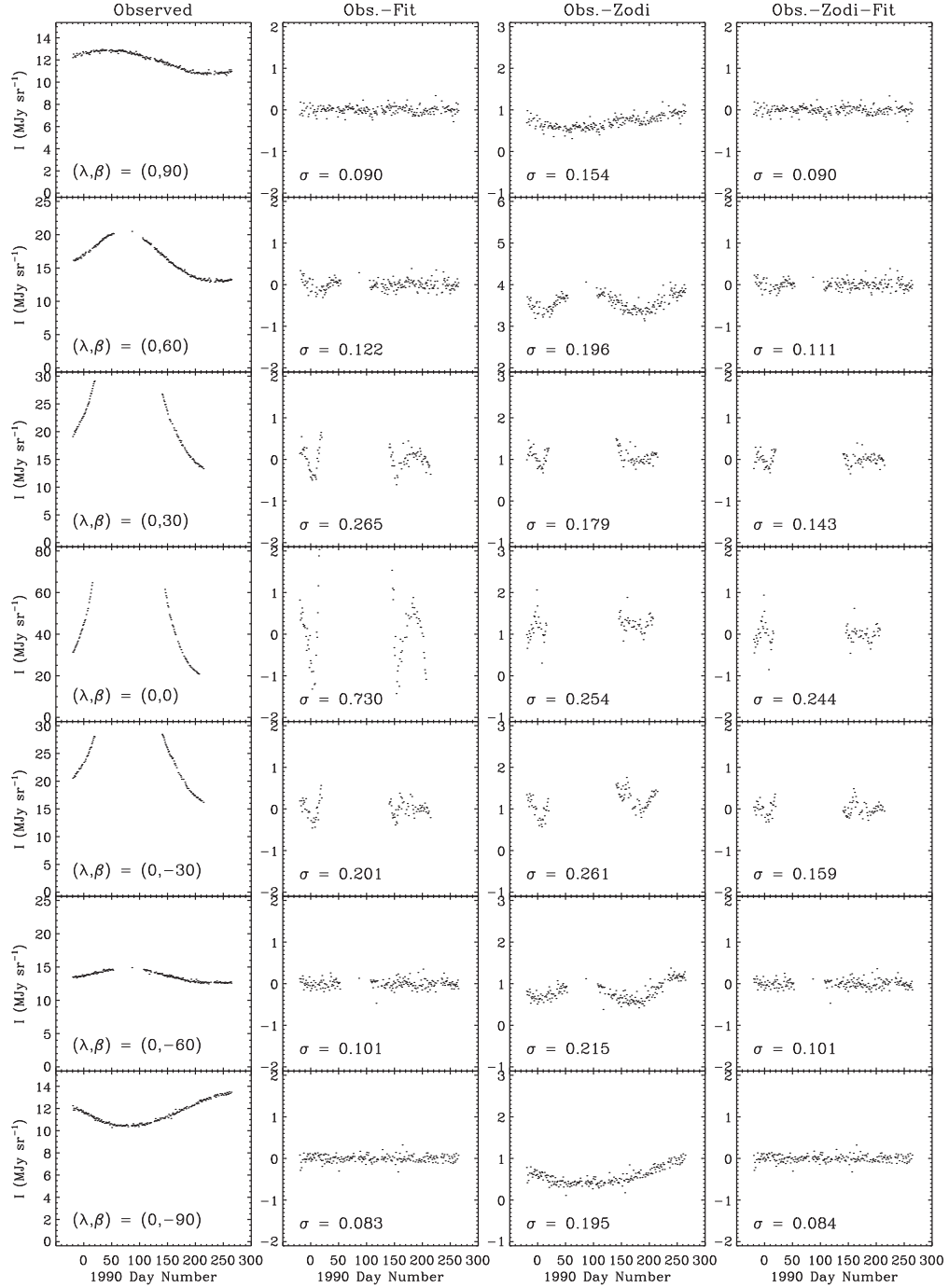
Wright, E. L. 1998, ApJ, 496, 1

Fig. 1.— The temporal variation of the 12 μm brightness at representative ecliptic latitudes. The left column shows the observed sky brightness. The second column shows the brightness after subtraction of a simple empirical fit to the variation at each pixel (Eq. 1). The third column shows the residual variation after the Kelsall et al. (1998) zodiacal light model is subtracted from the observations. The last column shows the results after application of Eq. 1 to the residual variation after subtraction of the zodiacal light model. The ecliptic coordinates of the fields are noted in the first column. The standard deviation of the residual variations (in MJy sr^{-1}) are listed in the other columns. Subtraction of both the zodiacal light model and the low frequency fit to the residuals is needed to minimize variations at all latitudes.
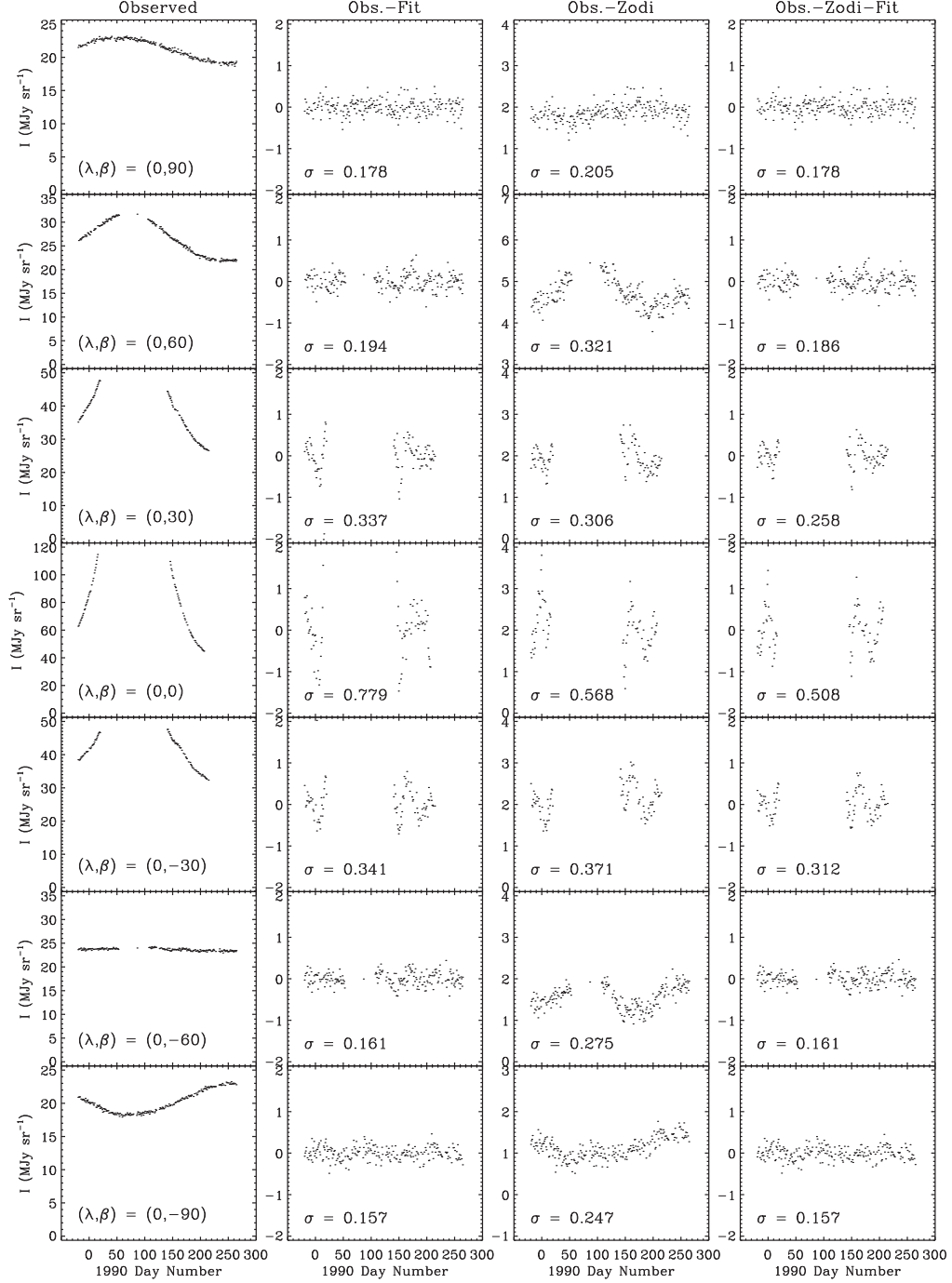
Fig. 2.— Temporal variations and residual emission at 25 μm, as described in Fig. 1

Fig. 3.— Still frame (Day 90179) from 12 μm residual movie in sky cube format, with an ecliptic coordinate grid superimposed. The trail of 2P/Encke is faintly visible across the SEP (between the blue tick marks). This image is scaled linearly from -0.5 to 0.5 MJy sr^{-1}. The 12 μm movies without and with annotation are shown in (a) and (b). The corresponding 25 μm movies are in (c) and (d).
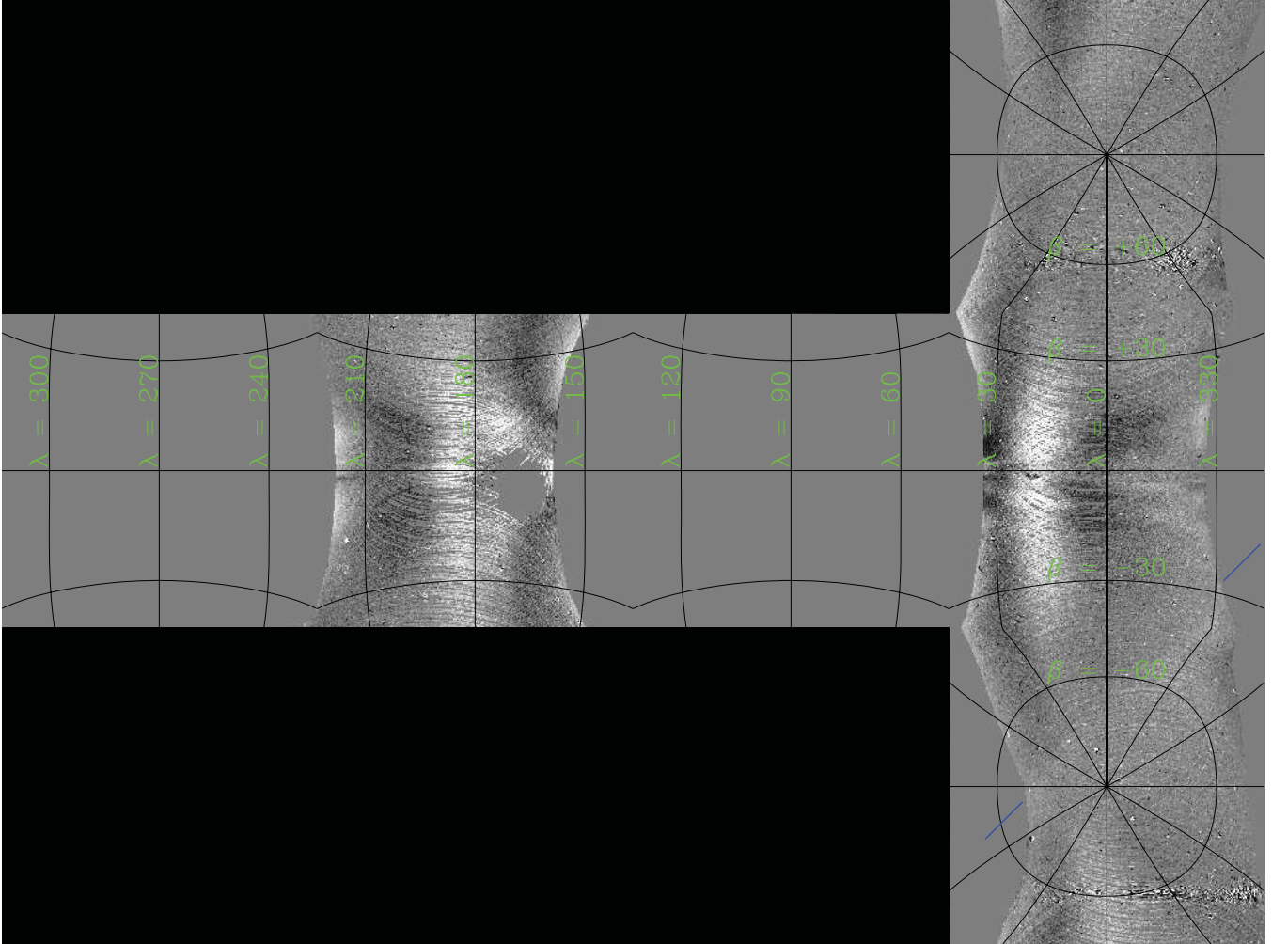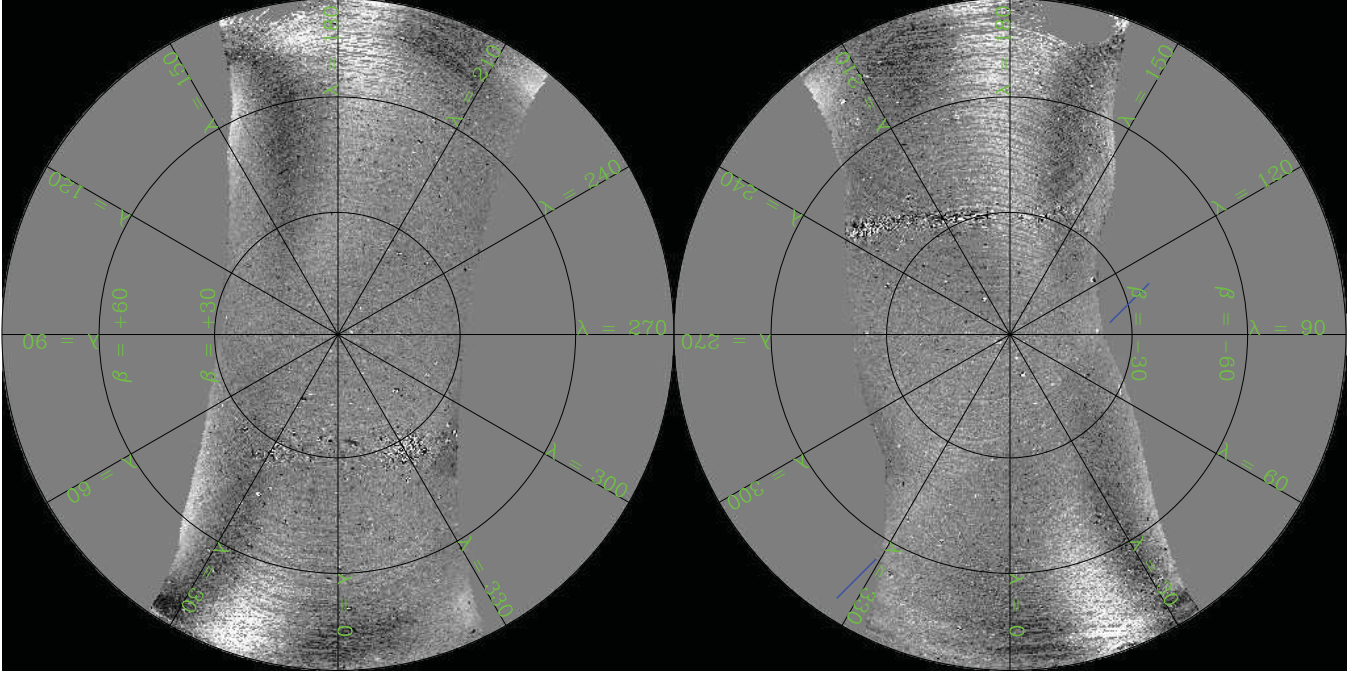
Fig. 4.— Still frame (Day 90179) from 12 μm residual movie in polar format, with an ecliptic coordinate grid superimposed. The trail of 2P/Encke is faintly visible across the SEP (between the blue tick marks). This image is scaled linearly from -0.5 to 0.5 MJy sr^{-1}. The 12 and 25 μm movies are shown in (a) and (b). Additional "cutouts" from the 12 μm movie loop back-and-forth over short intervals to highlight the motions of the trails of (c) 1P/Halley, (d) 2P/Encke, (e) 73P/SW3, (f) and (g) 169P/NEAT, (h) and (i) 3200 Phaethon.

Fig. 5.— Comet orbits projected on the ecliptic plane. 1P/Halley = red, 2P/Encke = Orange, 73P/SW3 = green, 169P/NEAT = cyan, 3200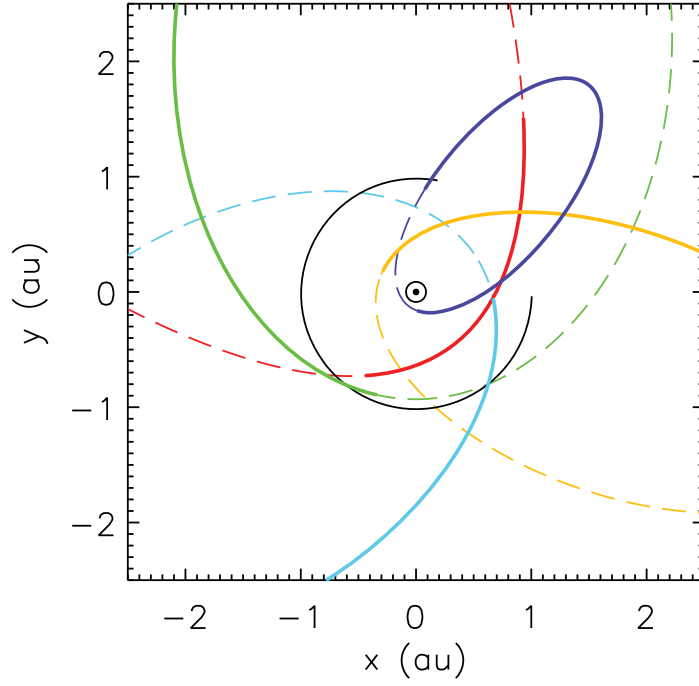 Phaethon = violet. Dashed lines indicate portions of orbits south of the ecliptic plane. Earth's orbit (black) is only shown for duration of the *COBE* cryogenic mission from 89345 - 90264. The dust trails are usually most visible at these orbital crossings.
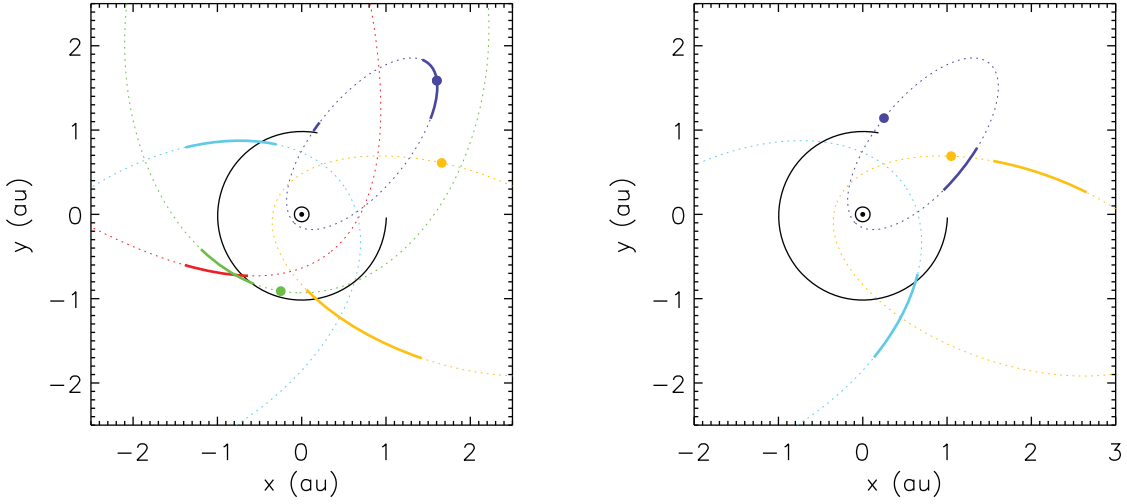
Fig. 6.— Portions of the orbits where the dust trails are evident are indicated by colored solid lines. 1P/Halley = red, 2P/Encke = Orange, 73P/SW3 = green, 169P/NEAT = cyan, 3200 Phaethon = violet. Dotted lines indicate portions of orbits that were not observed or where the trails were not evident. Earth's orbit (black) is only shown for duration of the *COBE* cryogenic mission from 89345 - 90264. The left panel shows sightings of the trails at dates prior to ∼90210, the right panel shows after that date. In each case the trail is only visible for several days when the Earth is near the location where the trail crosses the Earth's orbit (or nearest the visible trail segment). Visibility of the trails at small heliocentric radii is generally limited by DIRBE's elongation limit $\epsilon > 64°$. The visibility limits at large radii are subjective and very uncertain. Locations of the parent bodies (if within the limits of the figure) are marked as solid dots.

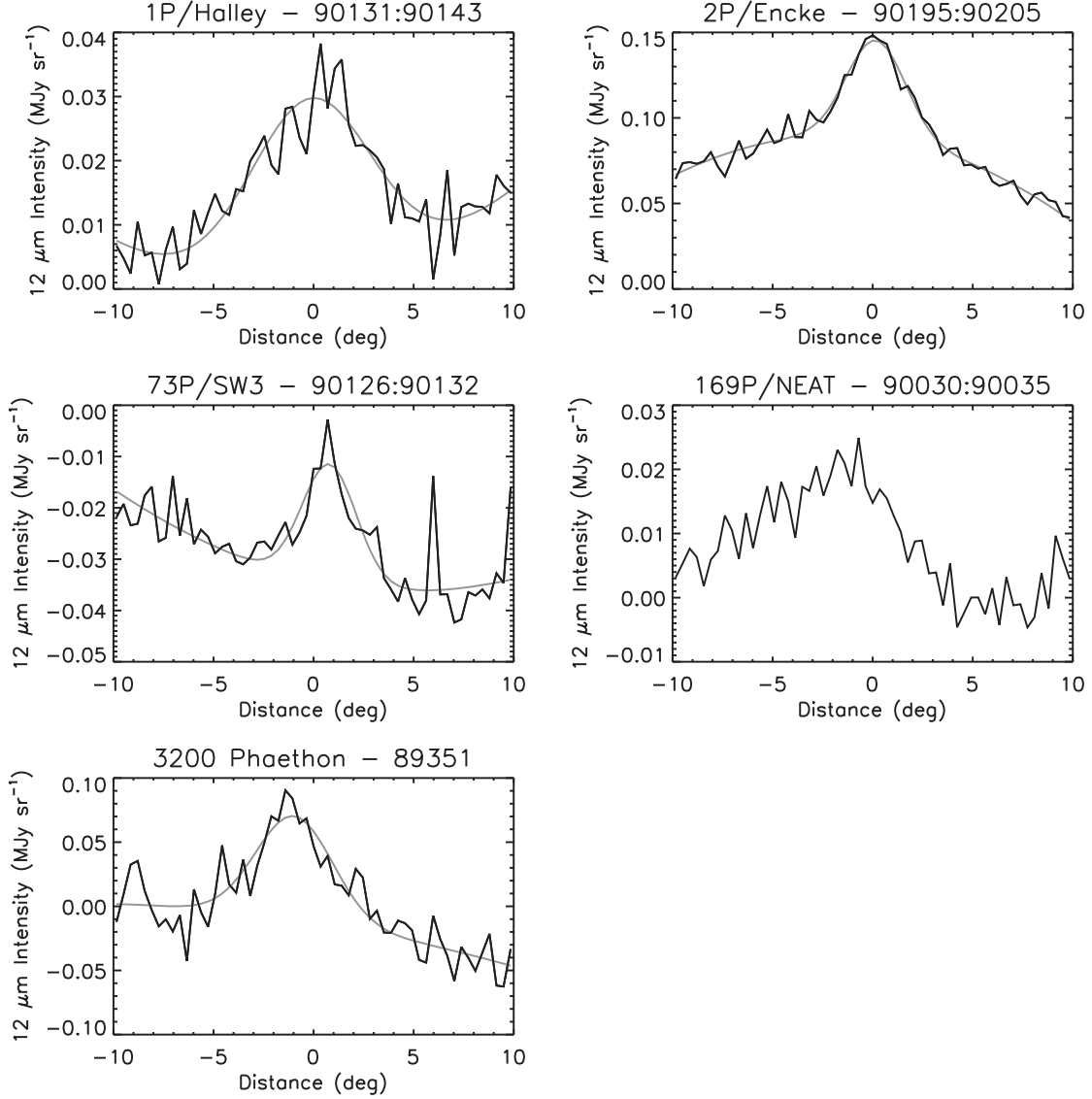Fig. 7.— Mean 12 μm profiles of the detected dust trails at the dates indicated. The gray lines indicated fits using a Gaussian profile and a second-order polynomial background (Eq. 1). The parameters of the fits are given in Table 4.
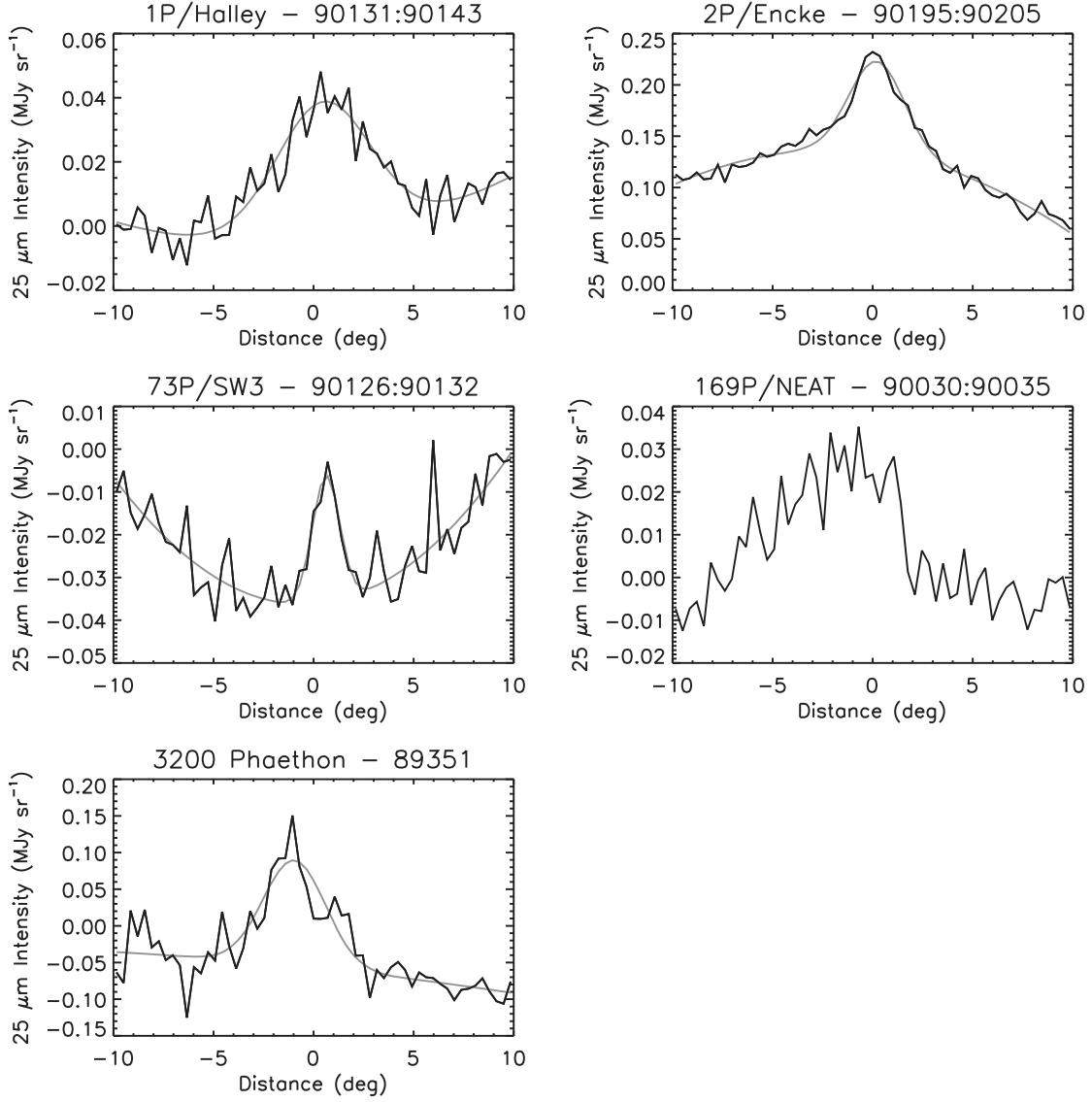
Fig. 8.— Mean 25 μm profiles of the detected dust trails, as in Fig. 7.

Table 1.   Moving Solar System Objects Detected by DIRBE

Planet	Reference	Asteroid	Reference	Comet	Reference
Mars	DIRBE[1]	1 Ceres	DIRBE[1]	73P/Schwassmann-Wachmann 3	Lisse et al. (1998)
Jupiter	DIRBE[1]	2 Pallas	DIRBE[1]	C/1989 Q1 (Okazaki-Levy-Rudenko)	Lisse et al. (1998)
Saturn	DIRBE[1]	4 Vesta	DIRBE[1]	C/1989 T1 (Helin-Roman-Alu)	new
		15 Eunomia	new	C/1989 X1 (Austin)	Lisse et al. (1998)
		31 Euphrosyne	new	C/1990 K1 (Levy)	Lisse et al. (1998)
		41 Daphne	new		
		42 Isis	new		
		85 Io	new		
		185 Eunike	new		
		194 Prokne	new		
		372 Palma	new		
		405 Thia	new		
		511 Davida	new		
		704 Interamnia	new		
		747 Winchester	new		
		1021 Flammario	new		

[1]DIRBE Solar System Objects Data: `http://lambda.gsfc.nasa.gov/product/cobe/dirbe_products.cfm`

Table 2.   DIRBE Comet Trails at Lines of Nodes

	1P/Halley	2P/Encke	73P/SW3	169P/NEAT	3200 Phaethon
Ascending Node Date	$\cdots$	**90240**	$\cdots$	90076	90168
Ascending Δr (au)	$\cdots$	**2.94**	$\cdots$	1.71	-0.87
Dates Detected	$\cdots$	**90233-90257?**	$\cdots$	none	$\epsilon < 64°$
Mean Anomaly Range[a] (°)	$\cdots$	**302.6 − 332.8**	$\cdots$	$\cdots$	$\cdots$
Meteor Shower	$\cdots$	$\cdots$	$\cdots$	$\cdots$	$\cdots$
Descending Node Date	**90140**	90054	**90152**	90262	**89351**
Descending Δr (au)	**-0.16**	-0.65	**-0.06**	-0.33	**-0.09**
Trail Detected	**90126-90142**	$\epsilon < 64°$	**90145-90154?**	none ($\epsilon < 66°$)	**89349-89357**
Mean Anomaly Range[a] (°)	**0.48 − 0.97**	$\cdots$	**358.7 − 360.0?**	$\cdots$	**328.4 − 333.2 & 90.0-200.0**
Meteor Shower	$\cdots$	$\cdots$	τ Herculids	$\cdots$	$\cdots$

[a]Minimum and maximum mean anomaly (measured from perihelion) at which a dust trail is visible during the dates listed.

Table 3.   DIRBE Comet Trails at Projected Earth Orbit Crossing (NEP or SEP)

	1P/Halley	2P/Encke	73P/SW3	169P/NEAT	3200 Phaethon
Inbound Date	$\cdots$	$\cdots$	**90134**	**90212**	89348
Inbound Δz (au)	$\cdots$	$\cdots$	**+0.06**	**+0.15**	+0.02
Inbound Detected	$\cdots$	$\cdots$	**90084-90136**	**90206-90224**	none?
Mean Anomaly Range[a] (°)	$\cdots$	$\cdots$	**348.6 − 355.4**	**335.4 − 350.2**	$\cdots$
Meteor Shower	$\cdots$	$\cdots$	$\cdots$	α Capricornids	Geminids
Outbound Date	**90127**	**90183**	90212	**90019**	$\cdots$
Outbound Δz (au)	**-0.07**	**-0.17**	-0.17	**-0.17**	$\cdots$
Outbound Detected	**90126-90142**	**90143-90211**	none	**90010-90040**	**90243-90264**
Mean Anomaly Range[a] (°)	**0.48 − 0.97**	**11.1 − 41.9**	$\cdots$	**8.4 − 21.8**	**23.4 − 61.8**
Meteor Shower	η Aquariids	Daytime ζ Perseids	$\cdots$	Daytime χ Capricornids	$\cdots$

[a]Minimum and maximum mean anomaly (measured from perihelion) at which a dust trail is visible during the dates listed.

Table 4.   DIRBE Comet Trail Profiles

	1P/Halley	2P/Encke	73P/SW3	169P/NEAT	3200 Phaethon
q (au)	0.586	0.336	0.933	0.607	0.140
i (°)	162.26	11.78	11.42	11.31	22.18
P (yr)	75.32	3.30	5.34	4.20	1.43
T_p (Julian)	2446467.4	2448193.1	2448031.6	2447491.0	2448196.1
T_p (Yr, Day)	86037	90302	90139	88330	90305
Dates Averaged	90131-90143	90195-90205	90126-90132	90030-90035	89351
Length Averaged (°)	66.4	43.9	105.1	55.5	27.8
R Range (au)	$0.97 - 1.54^a$	$0.92 - 1.14$	$1.02 - 1.14$	$1.03 - 1.18$	$1.01 - 1.05$
Δ Range (au)	$0.14 - 0.93^a$	$0.31 - 0.42$	$0.08 - 0.32$	$0.24 - 0.25$	$0.07 - 0.11$
θ_{LOS} Range (°)	$0 - 40$	$13 - 34$	$10 - 64$	$26 - 44$	$0 - 1$
Mean Anomaly Range (°)	$0.48 - 0.97^a$	$11.2 - 15.2$	$351.7 - 354.6$	$10.9 - 13.6$	$330.9 - 332.9$
Comet Mean Anomaly (°)	20.4	330.4	358.1	101.7	141.9
12 μm Profile					
I_0 (MJy sr^{-1})	0.029	0.057	0.023	$\cdots$	0.081
FWHM $\approx 2.35\sigma_\theta$ (°)	7.1	3.5	3.3	$\cdots$	4.5
θ_0 (°)	-0.10	0.16	0.78	$\cdots$	-0.96
C_0 (MJy sr^{-1})	0.00094	0.088	-0.034	$\cdots$	-0.013
C_1 (MJy sr^{-1})	0.00040	-0.0013	-0.00088	$\cdots$	-0.0024
C_2 (MJy sr^{-1})	0.00011	-0.00036	8.9e-05	$\cdots$	-9.5e-05
25 μm Profile					
I_0 (MJy sr^{-1})	0.042	0.089	0.030	$\cdots$	0.144
FWHM $\approx 2.35\sigma_\theta$ (°)	5.7	3.3	1.6	$\cdots$	3.8
θ_0 (°)	0.50	0.21	0.63	$\cdots$	-0.96
C_0 (MJy sr^{-1})	-0.0039	0.13	-0.036	$\cdots$	-0.057
C_1 (MJy sr^{-1})	0.00072	-0.0024	0.00033	$\cdots$	-0.0028
C_2 (MJy sr^{-1})	0.00013	-0.00056	0.00033	$\cdots$	-6.3e-05

Table 4—Continued

	1P/Halley	2P/Encke	73P/SW3	169P/NEAT	3200 Phaethon
Dates Averaged	$\cdots$	90233-90245	$\cdots$	90208-90218	90241-90264
Length Averaged (°)	$\cdots$	61.9	$\cdots$	64.3	39.7
R Range (au)	$\cdots$	$1.13 - 2.43$	$\cdots$	$1.06 - 2.09$	$0.93 - 2.18$
Δ Range (au)	$\cdots$	$1.16 - 1.72$	$\cdots$	$0.17 - 1.55$	$0.55 - 1.81$
θ_{LOS} Range (°)	$\cdots$	$0 - 1$	$\cdots$	$4 - 66$	$10 - 61$
Mean Anomaly Range (°)	$\cdots$	$311.7 - 344.9$	$\cdots$	$327.3 - 348.5$	$24.0 - 113.6$
Comet Mean Anomaly (°)	$\cdots$	342.1	$\cdots$	144.1	325.4
12 μm Profile					
I_0 (MJy sr^{-1})	$\cdots$	0.050	$\cdots$	$\cdots$	0.016
FWHM $\approx 2.35\sigma_\theta$ (°)	$\cdots$	3.3	$\cdots$	$\cdots$	3.1
θ_0 (°)	$\cdots$	-0.83	$\cdots$	$\cdots$	1.01
C_0 (MJy sr^{-1})	$\cdots$	0.037	$\cdots$	$\cdots$	0.026
C_1 (MJy sr^{-1})	$\cdots$	-0.00074	$\cdots$	$\cdots$	-0.0027
C_2 (MJy sr^{-1})	$\cdots$	-7.3e-05	$\cdots$	$\cdots$	8.7e-05
25 μm Profile					
I_0 (MJy sr^{-1})	$\cdots$	0.099	$\cdots$	$\cdots$	0.034
FWHM $\approx 2.35\sigma_\theta$ (°)	$\cdots$	3.5	$\cdots$	$\cdots$	2.4
θ_0 (°)	$\cdots$	-0.79	$\cdots$	$\cdots$	0.93
C_0 (MJy sr^{-1})	$\cdots$	0.0047	$\cdots$	$\cdots$	0.039
C_1 (MJy sr^{-1})	$\cdots$	-0.0031	$\cdots$	$\cdots$	-0.0045
C_2 (MJy sr^{-1})	$\cdots$	-0.00021	$\cdots$	$\cdots$	0.00014

Note. — q = perihelion dist., i = inclination, P = period, T_p = Date of perihelion; **Dates Averaged** = range of dates averaged to generate profile (not necessarily when trail is closest, nor all visible dates), **Length Averaged** = projected angular length of the trail averaged to generate profile, R **Range** = range of heliocentric distance within length of trail averaged (varies slightly with date), Δ **Range** = range of geocentric distance within length of trail averaged (varies slightly with date), θ_{LOS} **Range** = range of angle between LOS and orbital plane (varies with date and position along trail), **Mean Anomaly Range** = range of mean anomaly measured from perihelion within length of trail averaged (varies slightly with date), **Comet Mean Anomaly** = Mean anomaly of the parent body measured from perihelion (varies slightly with date); **profile fit** = $I_0 \exp\left[-0.5(\theta - \theta_0)^2/\sigma_\theta^2\right] + C_0 + C_1\theta + C_2\theta^2$

[a]Stated ranges are truncated at the tangent point of the orbit.